*Journal of The Electrochemical Society*, **160** (6) A968-A972 (2013)
0013-4651/2013/160(6)/A968/5/$31.00 © The Electrochemical Society

# Molecular Dynamics Simulations of SOC-Dependent Elasticity of $Li_xMn_2O_4$ Spinels in Li-Ion Batteries

**Seungjun Lee,[a] Jonghyun Park,[a] Ann Marie Sastry,[b] and Wei Lu[a,z]**

[a]*Department of Mechanical Engineering, University of Michigan, Ann Arbor, Michigan 48109, USA*
[b]*Sakti3, Ann Arbor, Michigan 48108, USA*

As has been experimentally observed, stresses due to lithium intercalation, phase transition, and thermal loading can cause local fractures in Li-ion battery active materials. These fractures are one of the main degradation mechanisms in Li-ion batteries. Consequently, predicting the stress level inside of the electrode material is of key importance in designing cells and determining their operation conditions. For lithium manganese oxides, however, the values of Young's modulus that have been reported so far differ widely, resulting in commensurately wide gaps between actual and predicted stress levels. Moreover, little is known about how the Young's modulus changes at different states of charge (SOC). In this study, molecular dynamics (MD) simulations were performed to investigate the Young's moduli of $Li_xMn_2O_4$ as a function of SOC ($0 < x < 1$). MD simulations show that the Young's moduli vary almost 18% depending on SOC. By decomposing interaction forces between atoms, we analyzed how pair interactions influence the variance. The results suggest that the SOC-dependence of Young's modulus may have an effect on both the stress level inside the particle as well as on Li-ion transport as a result of their mutual coupling to Li-ion diffusivity.
 [DOI: 10.1149/2.147306jes] 

Manuscript submitted March 1, 2013; revised manuscript received April 8, 2013. Published April 20, 2013.

Lithium manganese oxide is currently widely used in commercial Li-ion batteries; it is preferred over lithium cobalt oxide and lithium nickel oxide due to its high voltage, low cost and environmental compatibility.[1–3] This material, however, shows a large volume change during lithium intercalation and deintercalation, which induces stress resulting in fracture inside the electrode. Further, it is a brittle material, which makes it vulnerable to stress-buildup, and thus fracture in lithium manganese oxides is one concern that needs to be addressed in order for battery performance to be improved. Mechanical damage of active materials will degrade battery performance and life because it accelerates the dissolution of active materials and the formation of a new interface between the solid and the electrolyte. As discussed many times in the literature,[4–6] fracture is a key degradation mechanism in Li-ion batteries. Further, stress is strongly coupled to the Li-ion diffusion process. This implies that the accurate prediction of stress fields inside particles is critical to predicting battery performance. Extensive efforts have been focused on developing mathematical models for the diffusion-induced stress field in $Mn_2O_4$ hosts upon Li intercalation. In these numerical analyzes, Young's modulus is essential as an input parameter. However, there are two concerns regarding the values of Young's modulus used in the previous studies. One is that these previously used values differ significantly, ranging from 10 GPa to 200 GPa[4,5,7–9] for a fully intercalated $LiMn_2O_4$ due to various experimental techniques used. The other is that the values of Young's modulus are treated as constant upon lithiation. However, the amount of Li may alter the mechanical properties. The usage of different elasticity values strongly affects the stress level in lithium manganese oxides; for example, it has been pointed out that the maximum tensile stress in an active particle increases more than five times when Young's modulus increases from 10 GPa to 100 GPa.[9]

A variety of Young's modulus usage stems from a wide range of reported values. Using the reed vibration technique, the Young's modulus of $LiMn_2O_4$ has been measured as 10 GPa[10] and 25 GPa.[11] Several experiments using the X-ray diffraction technique have reported the bulk modulus of $LiMn_2O_4$ to be 100 GPa[12] and 119 GPa.[13] In addition to experiments, a theoretical study using ab initio calculations has obtained a 200 GPa bulk modulus.[14] For elastically isotropic materials, bulk modulus $K$ can be converted to Young's modulus $E$ with $E = 3K(1 - 2\nu)$, where $\nu$ is Poisson's ratio. The estimated Young's moduli are 120 GPa, 143 GPa, and 240 GPa using 100 GPa, 119 GPa, and 200 GPa bulk moduli, respectively, by taking $\nu = 0.3$. Namely, the reported values from experiments and theoretical calculations vary from 10 GPa to 240 GPa, showing one order of magnitude difference.

The inserted Li may alter the mechanical properties of LMO materials, as shown in other battery materials such as $Li_xFePO_4$[15] and graphite.[16] The reason for such little information about SOC-dependent properties is due to experimental difficulty in controlling exact SOCs.[16]

Performing atomistic simulations is a technique capable of revealing features in such limited environments. In this study, we performed molecular dynamics (MD) simulations to investigate the SOC-dependent Young's modulus of $Li_xMn_2O_4$ in range of $0 < x < 1$. Although the theoretical study using ab initio calculations[14] has been performed at $x = 0.0$, 0.5 and 1.0, it was not sufficient to show experimental observations such as change in lattice constants and volume expansion during Li intercalation. Due to the complexity of a LMO crystal structure, the optimization of crystal structures at a given SOC needs to be carefully investigated. For example, when Li-ions intercalate into a $Li_xMnO_2$ host ($x = 0.5$), the number of cases in which they can be arranged at vacant sites is huge. It is very difficult to test all possible cases and find the optimized structure where energy is minimized by ab initio calculations due to computational cost. In contrast to ab initio calculations, MD simulations allow efficient testing of energy levels for numerous configurations using predefined potential equations. In addition to methodological efficiency, the MD simulations in this work effectively demonstrated SOC-dependent lattice constants, phase transition, and volume expansion, which have been observed in several experiments.[17–20] Further, it is found that the calculated elasticity of $Li_xMn_2O_4$ ($0 < x < 1$) varies as a function of SOC. This may affect the stress level due to Li intercalation and the diffusion process of Li-ions inside the particle.

The paper is structured as follows: In Section 2, the method of MD simulations and the calculation of Young's modulus are described. In Section 3, validation for the used potential is conducted by comparing the calculated lattice constants with experimental measurements. The SOC-dependent elastic properties of $Li_xMn_2O_4$ are presented next, followed by an analysis of the change in Young's modulus at different SOC by decomposing the calculated values. In Section 4, the findings are summarized.

## Methods

*MD simulations.*— Pair interactions between atoms are described by a Gilbert-Ida-type pair potential function:[21]

$$U(r_{ij}) = \frac{Z_i Z_j e^2}{r_{ij}} + f_0 \times (b_i + b_j) \exp\left(\frac{a_i + a_j - r_{ij}}{b_i + b_j}\right), \quad [1]$$

where the first term represents electrostatic interactions and the second term represents exchange repulsion interactions. $Z_i$ is the atomic

[z]E-mail: weilu@umich.edu

**Table I. Potential parameters used in Equation 1.**

| Ions | $Z_i$ | $a_i$(Å) | $b_i$(Å) |
|---|---|---|---|
| $Li^+$ | +1.0 | 1.043 | 0.080 |
| $Mn^{3+}$ | +1.4 | 1.038 | 0.070 |
| $Mn^{4+}$ | +2.4 | 0.958 | 0.070 |
| $O^{2-}$ | −1.2 | 1.503 | 0.075 |

charge of atom $i$, $e$ is the elementary electric charge, $r_{ij}$ is an interatomic distance between atom $i$ and atom $j$, $f_0$ is a constant (4.184 kJÅ$^{-1}$mol$^{-1}$), $a_i$ is the atomic radius and $b_i$ is the atomic compressibility. Potential parameters derived by Suzuki et al.[22] are used and listed in Table I. These parameters have been used in previous studies to successfully explain a wide range of experimental observations in lithium manganese oxide spinels.[22–24] Other potential functions such as Lennard-Jones potential and Morse potential may describe pair interactions similarly well or even better. However, it is not easy to fit the interactions in the LMO system and the available parameters for LMO are limited in the literature. To ensure the capability of the potential functions and parameters, we will show that the lattice constants calculated from the potential we used agree well with experimental measurement.

The unit cell of $LiMn_2O_4$ considered in our simulations is shown in Fig. 1. It contains 56 ions (8 lithium atoms, 16 manganese atoms and 32 oxygen atoms) and the length of one side is 8 Å approximately: the exact length depends on SOC. Nine SOC cases are considered: x = 1.0, 0.875, 0.75, 0.625, 0.5, 0.375, 0.25, 0.125 and 0.0 in $Li_xMn_2O_4$. As the number of Li decreases, the same number of $Mn^{3+}$ is switched to $Mn^{4+}$ in order to maintain system neutrality.

All MD simulations are performed using LAMMPS.[25] The exponential form in Eq. 1 is properly transformed to fit into the Buckingham potential form. The long-range Coulomb forces are computed using the Ewald method. The isothermal-isobaric (NPT) ensemble is used during the equilibrium process and the canonical ensemble (NVT) is used while a strain is applied. Temperature is kept constant at 300 K using the Nosé-Hoover thermostat. The time step is set to 1 fs. Periodic boundary conditions are used in all directions.

Simulations are performed in two steps. First, optimized structures are found at each SOC. In the $Li_xMn_2O_4$ system, the Li-ions are positioned on the 8a tetrahedral sites, and the manganese ions are located on the 16d octahedral sites. All possible initial configurations with a combination of $Li^+$, $Mn^{3+}$ and $Mn^{4+}$ are constructed. For example, for x = 0.125, the number of $Li^+$ is one and the number of available sites for $Li^+$ is eight. For the manganese ions, one $Mn^{3+}$ and fifteen $Mn^{4+}$s occupy sixteen sites. Thus, the total number of crystal configurations is 128. In this way the number of cases for x = 0.250, 0.375, 0.500, 0.625, 0.750, 0.875 and 1.00 is 3,360, 31,360, 127,400, 244,608, 224,224, 91,520 and 12,870, respectively. Here a large number of cases for each SOC are resulted from the intrinsic MD methodology that treats $Li^+$, $Mn^{3+}$ and $Mn^{4+}$ as different atoms. Since it is almost impossible to check the equilibrium energy of all these cases, we calculate the potential energy of these initial configurations by running one time step of MD simulations and sort the cases according to energy levels. We randomly choose cases at low energy states (within 30 eV from the lowest energy) and equilibrate them because low initial energy states have a higher chance of reaching low equilibrium energy states. After the selected structures are equilibrated, we only collect cases in which the equilibrium energy belongs within 5 eV of the lowest energy at each SOC.

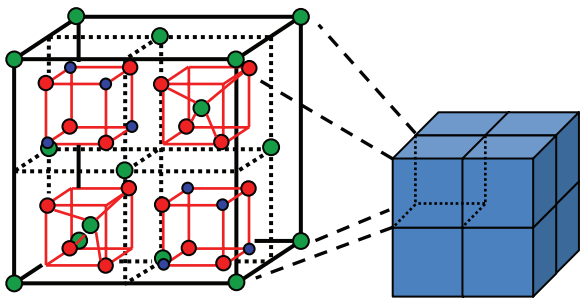

**Figure 1.** (Color online) Schematic of a lattice structure of $LiMn_2O_4$: a unit cell (left side, shown with the front-half of the atoms inside) including lithium (green), manganese (blue) and oxygen (red) and a 2 × 2 × 2 cubic structure for MD simulations (right side).

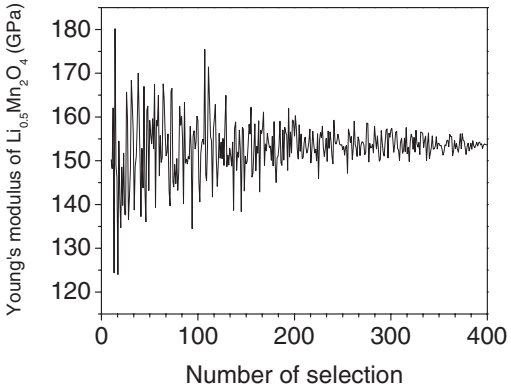


**Figure 2.** Convergence of Young's modulus ($Li_{0.5}Mn_2O_4$) with the increase of points selected for applying a strain.

After the optimized structures are collected, three structures are chosen randomly at each SOC, and a strain of 0.5% is applied to these structures by increasing the size of the simulation box. As the system is strained, the positions of atoms are linearly relocated along the strained directions. After straining, the system is equilibrated for another 10 ps.

Although we apply the strain to the equilibrated system, the resultant stresses fluctuate depending on which equilibrium point is chosen. In order to obtain a converged stress, convergence tests are conducted by increasing the number of selections. We find that 400 points are enough to reach convergence. Figure 2 shows a representative result for x = 0.5 in $Li_xMn_2O_4$. In addition to the convergence test, the effect of the system size is examined. At least two unit cells are needed in one side of the simulation box because the cutoff distance for pair interactions is set to 10 Å, which exceeds one unit cell of 8 Å. The unit cell is duplicated in order to construct the whole domain. As the system size increases, the fluctuation of stress decreases; consequently, fewer points are needed for convergence. Computation time increases considerably at the same time, however. Thus, a tradeoff is needed between system size and computation time. After the convergence tests are conducted with a larger system size, a smaller system size of 2 × 2 × 2 unit cells is selected, where the computation time cost the least (although larger points (400) are needed to be simulated). For each selected point, four different simulations are performed: three uniaxial deformations in the x, y, z directions and one hydrostatic deformation.

Stresses are calculated in the form of the virial stress. The stress is expressed as[26]

$$\boldsymbol{\sigma}(\mathbf{r}) = \frac{1}{\Omega}\sum_i \left[ -m_i \dot{\mathbf{u}}_i \otimes \dot{\mathbf{u}}_i + \frac{1}{2}\sum_{j\neq i} \mathbf{r}_{ij} \otimes \mathbf{f}_{ij} \right], \qquad [2]$$

where Ω is the total volume, $m_i$ is the mass of atom $i$, $\dot{\mathbf{u}}_i$ is the time derivative of $\mathbf{u}_i$, which denotes the displacement vector of atom $i$ relative to a reference position, $\mathbf{r}_{ij} = \mathbf{r}_j - \mathbf{r}_i$, ⊗ is the cross product, and $\mathbf{f}_{ij}$ is the interatomic force applied on atom $i$ by atom $j$.

*Linear elastic relation.*— For a linear elastic stress-strain relation, the generalized constitutive relation during an axial tensile test can be

written as

$$\begin{Bmatrix} \sigma_{11} \\ \sigma_{22} \\ \sigma_{33} \end{Bmatrix} = \begin{bmatrix} C_{11} & C_{12} & C_{13} \\ C_{12} & C_{22} & C_{23} \\ C_{13} & C_{23} & C_{33} \end{bmatrix} \begin{Bmatrix} \varepsilon_{11} \\ \varepsilon_{22} \\ \varepsilon_{33} \end{Bmatrix}, \quad [3]$$

where $\sigma_{ij}$, $\varepsilon_{ij}$, $C_{ij}$ are the stress, strain and elastic constant, respectively.[27] For uniaxial deformation ($\varepsilon_{22} = \varepsilon_{33} = 0, \varepsilon_{11} \neq 0$), the normal stress in the x direction becomes $\sigma_{11} = C_{11}\varepsilon_{11}$, thus

$$C_{11} = \frac{\sigma_{11}}{\varepsilon_{11}}. \quad [4]$$

The elastic bulk modulus $K$ can be calculated by

$$K = \frac{1}{3}\left(\frac{\sigma_{11} + \sigma_{22} + \sigma_{33}}{\varepsilon_{11} + \varepsilon_{22} + \varepsilon_{33}}\right). \quad [5]$$

For hydrostatic deformation ($\varepsilon_{11} = \varepsilon_{22} = \varepsilon_{33}$), Equation 5 becomes

$$K = \frac{1}{9}\left(\frac{\sigma_{11} + \sigma_{22} + \sigma_{33}}{\varepsilon_{11}}\right). \quad [6]$$

Therefore, $C_{11}$ and $K$ can be obtained by the unidirectional deformation and the hydrostatic deformation, respectively. Both $K$ and $C_{11}$ can be expressed in terms of Young's modulus and Poisson's ratio for an isotropic material,

$$C_{11} = \frac{(1-\nu)E}{(1+\nu)(1-2\nu)}, \quad [7]$$

$$K = \frac{E}{3(1-2\nu)}. \quad [8]$$

Therefore from Eqs. 7 and 8, an effective Young's modulus can be evaluated by

$$E = \frac{9K(C_{11} - K)}{3K + C_{11}}. \quad [9]$$

## Results and Discussion

*Validation.*— The lattice constants of $Li_xMn_2O_4$ are measured for the optimized structures collected through the equilibrium process explained in session 2.1. The lattice constants are calculated by measuring the size of equilibrated systems. The calculated lattice constants are shown in Fig. 3. The averaged value at each SOC gradually decreases as the amount of lithium decreases and the overall trend agrees well with experimental observations.[17–20] The lattice constant varies from 8.237 Å for x = 1 to 8.044 Å for x = 0. The corresponding volume change is $(8.237^3 – 8.044^3) / 8.044^3 = 7\%$, which agrees with the reported 6.5% change of a LMO particle.[9] Another feature that we notice in Fig. 3 is a wider scatter of the lattice constants at x = 0.375 and 0.250. This is due to the existence of two phases, which matches with the general belief that there exist two phases in the range of low SOC. Good agreement with experimental measurements implies reliability of the interatomic potential used.

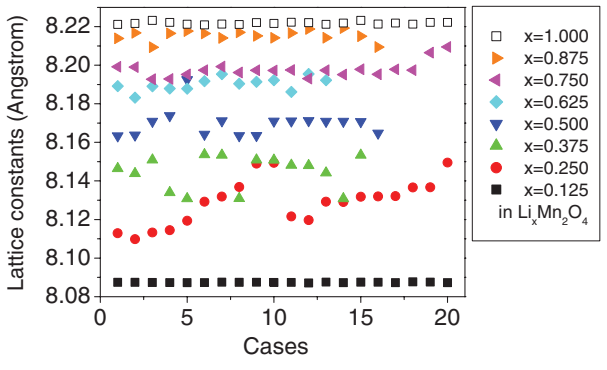


**Figure 3.** (Color online) Calculated lattice constants of $Li_xMn_2O_4$ at different SOCs. Shown are the cases where the equilibration energy is within 5 eV of the lowest energy at each SOC.

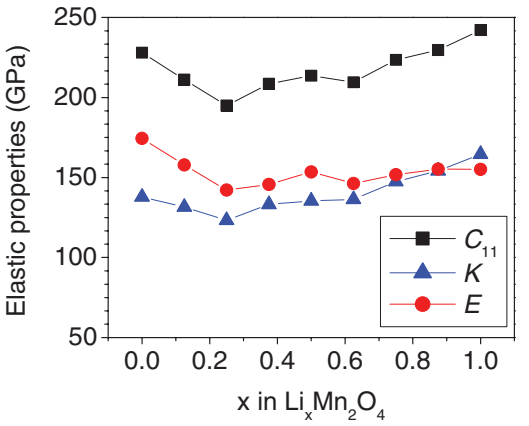


**Figure 4.** (Color online) Calculated elasticity constant $C_{11}$, bulk modulus $K$ and Young's modulus $E$ of $Li_xMn_2O_4$ as a function of x. The values are the average of the three cases at each SOC.

*Elastic modulus.*— The elastic properties are calculated for three crystal structures chosen from among a group of structures based on energy minimization at each SOC. The calculated values are averaged and shown in Fig. 4. The elastic constant $C_{11}$, bulk modulus $K$ and Young's modulus $E$ show a similar trend; as the state of charge decreases from 1 to 0.25 the elastic properties also decrease. As the state of charge decreases from 0.25 to 0 the elastic properties increase. The Young's modulus of $Li_xMn_2O_4$ is calculated as 155.1 GPa for x = 1. It drops to 142.2 GPa for x = 0.25 and increases up to 174.4 GPa for x = 0. The results indicate that the Young's modulus of $Li_xMn_2O_4$ changes by a maximum of 18% as a function of x. The variance of Young's moduli due to lithiation has also been reported in other spinel oxides, with the maximum of almost 50%.[28]

The calculated values are decomposed in order to investigate the elasticity variance of $Li_xMn_2O_4$ with Li contents. Because all three properties $C_{11}$, $K$ and $E$ show a similar trend, we decompose $C_{11}$ without losing generality. Figure 5 shows the decomposition of $C_{11}$. The elasticity constant $C_{11}$ is largely composed of three terms: the kinetic energy contribution, the long-range coulomb interaction and the pair interaction. As seen in Fig. 5, the kinetic energy contribution and the long-range coulomb interaction do not change much as a function of x. However, the curve of the pair interaction changes

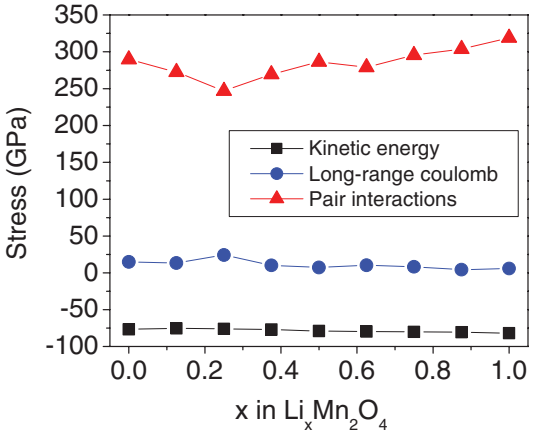


**Figure 5.** (Color online) Decomposition of $C_{11}$ into kinetic energy contributions, long-range coulomb interaction and pair interaction.

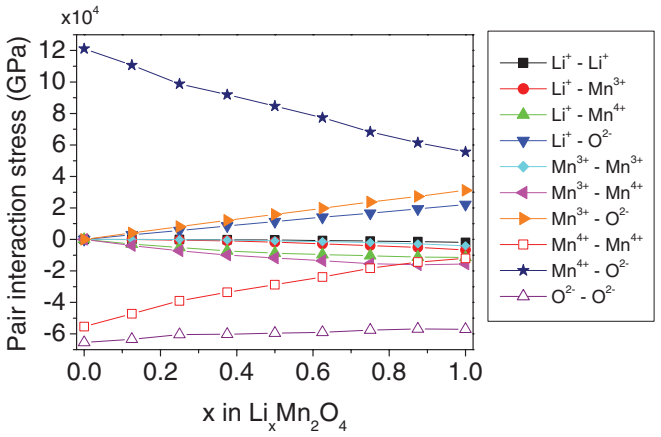


**Figure 6.** (Color online) Decomposition of the pair interaction into ten types of interactions.

and follows the trend of $C_{11}$. The pair interaction, once again, is decomposed for detailed investigation.

There are ten types of pair interactions in the system: $Li^+$ - $Li^+$, $Li^+$ - $Mn^{3+}$, $Li^+$ - $Mn^{4+}$, $Li^+$ - $O^{2-}$, $Mn^{3+}$ - $Mn^{3+}$, $Mn^{3+}$ - $Mn^{4+}$, $Mn^{3+}$ - $O^{2-}$, $Mn^{4+}$ - $Mn^{4+}$, $Mn^{4+}$ - $O^{2-}$ and $O^{2-}$ - $O^{2-}$. These pair interactions can be attractive (positive) or repulsive (negative) depending on pair potential expressed in Eq. 1. As the Li-ions intercalate, the amount of Li-ions, $Mn^{3+}$, and $Mn^{4+}$ changes, and relevant pair interactions also change. This variation determines the pattern of the $C_{11}$ curve. Figure 6 shows the decomposed stresses representing the ten interactions. In order to link to the variation of $C_{11}$, the pair interactions are divided into two groups according to their derivatives with respect to x in Fig. 7. As seen in Fig. 7a, the $Mn^{4+}$ - $O^{2-}$ interaction dominates the decline in the stress. Further, the magnitude of this derivative decreases as x increases. This is related to the distance between $Mn^{4+}$ and $O^{2-}$. As can be seen in Fig. 8, the overall average distance between $Mn^{4+}$ and $O^{2-}$ within the cutoff range is changed. This overall average distance is calculated by averaging all the distances between these two kinds of atoms within the cutoff range and over the entire calculated structure. It is not the nearest neighbor distance between these two atoms. The small overall average distance at the initial state explains the strong interaction between all $Mn^{4+}$ and $O^{2-}$ ions. The magnitude of the derivative decreases as x increases due to the decrease of the amount of $Mn^{4+}$ ions and the increase of the distance between $Mn^{4+}$ and $O^{2-}$; however, the $Mn^{4+}$ - $O^{2-}$ interaction still dominates throughout the whole region. Experimental observation shows that the average nearest neighbor distances of $Mn^{4+}$-$O^{2-}$ and $Mn^{3+}$- $O^{2-}$ are 1.98 Å and 1.88 Å, respectively.[29] Our simulations give the nearest neighbor distances to be 2.03 Å and 1.85 Å on average, which agree with experimental observations. For the positive derivative shown in Fig. 7b, the $Mn^{4+}$ - $Mn^{4+}$ interaction dominates at small SOCs. However, as the SOC increases, the reaction becomes weak due to the decrease of the amount of $Mn^{4+}$ ions. At high SOCs, the $Mn^{3+}$ - $O^{2-}$ and $Li^+$ - $O^{2-}$ interactions become important as the amount of $Mn^{3+}$ and $Li^+$ ions increases. Finally, the competition between the negative and positive derivatives determines the pattern of the $C_{11}$ curve. At low SOC, the interaction between $Mn^{4+}$ - $O^{2-}$ dominates. However, as Li intercalates further, the amount of $Mn^{4+}$ ions decreases, resulting in the decrease of the $Mn^{4+}$ – $O^{2-}$ interaction and the increase of the $Li^+$ - $O^{2-}$ and $Mn^{3+}$ - $O^{2-}$ interactions.

As we mentioned early, it is very difficult to find comparable data regarding the elasticity of $Li_xMn_2O_4$. The only available data is from ab initio calculations,[14] which report that the bulk modulus of $LiMn_2O_4$ is about 200 GPa, and that there is little variance at different states of oxidation. However, previous ab initio works have not properly captured the change in the lattice constants of the system and are unable to properly measure the bulk modulus. In addition, the recent study by Lin et al.[13] suggested that lithium manganese

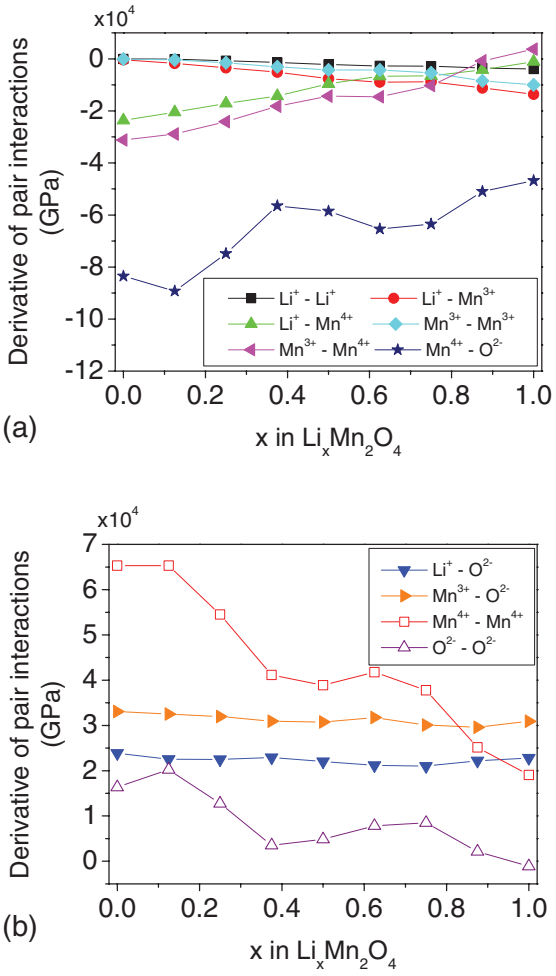


**Figure 7.** (Color online) Derivative of the decomposed pair interactions: (a) a group with negative derivatives and (b) a group with positive derivatives.

oxides can have a lower modulus than the bulk modulus 200 GPa, which is the modulus magnitude of similar oxide spinels such as $MgAl_2O_4$,[30] $NiMn_2O_4$,[31] $ZnMn_2O_4$[32] and $CuMn_2O_4$,[33] due to their higher compressibility.

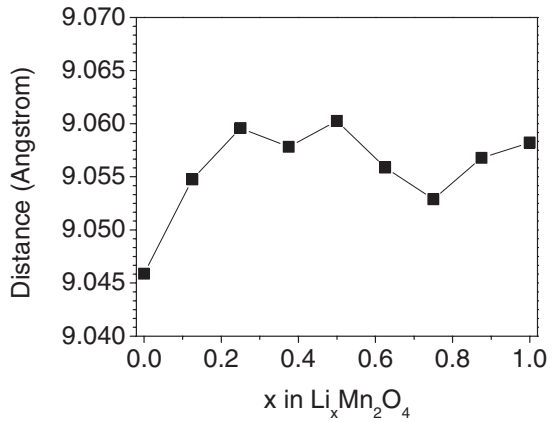


**Figure 8.** Overall average distance between all $Mn^{4+}$ and $O^{2-}$ atoms within the cutoff range.

## Conclusions

In this study, we calculated the elasticity of $Li_xMn_2O_4$ as a function of the state of charge using MD simulations. The Young's modulus of $Li_xMn_2O_4$ was calculated as 174.4 GPa for x = 0 and 155.1 GPa for x = 1. As the oxidation states change, the elasticity of $Li_xMn_2O_4$ changes by the maximum of 18%. As the state of charge decreases from 1 to 0.25, the Young's modulus of $Li_xMn_2O_4$ tends to decrease and increase again as the state of charge decreases from 0.25 to 0. We analyzed the reason for this trend by decomposing the calculated pair potentials. The decomposition shows that the trend results from the competition of pair interactions: the $Mn^{4+}$ - $O^{2-}$ interaction charges for the decreasing trend at low SOCs and $Li^+$ - $O^{2-}$ and $Mn^{3+}$ - $O^{2-}$ does for the increasing trend at high SOCs, and this change of pair interactions is due to the decreasing amount of $Mn^{4+}$ and the increasing amount of $Li^+$ and $Mn^{3+}$.

Our results suggest that the SOC-dependent elasticity of lithium manganese oxides should be considered in continuum models for more precise evaluation of stress levels and fracture issues in Li-ion batteries. Further, the stress field inside the particle affects the diffusion process of Li-ions. As a Li-ion intercalates into the host material, a stress field builds due to intercalated ion displacement of the host atoms. Next, this stress field affects the energy of the second intercalated ion, leading to an elastic interaction between the two ions. In addition, the SOC-dependency of Young's modulus implies that the chemical potential driving Li-ion diffusion inside the particle may be affected by the compliance variance as the Li-ion concentration changes. In light of the above, our findings from the MD calculation call for more detailed investigation into the coupling phenomena between stress field and diffusivity.

## Acknowledgement

This research was funded by the GM /UM Advanced Battery Coalition for Drivetrains. Support from our sponsors is gratefully acknowledged.

## References

1. J. Park, J. H. Seo, G. Plett, W. Lu, and A. M. Sastry, *Electrochemical and Solid-State Letters*, **14**, A14 (2011).
2. J. Cabana, T. Valdés-Solís, M. R. Palacín, J. Oró-Solé, A. Fuertes, G. Marbán, and A. B. Fuertes, *Journal of Power Sources*, **166**, 492 (2007).
3. J. M. Tarascon and M. Armand, *Nature*, **414**, 359 (2001).
4. M. Zhu, J. Park, and A. M. Sastry, *Journal of The Electrochemical Society*, **159**, A492 (2012).
5. W. H. Woodford, Y.-M. Chiang, and W. C. Carter, *Journal of The Electrochemical Society*, **157**, A1052 (2010).
6. Y. Hu, X. Zhao, and Z. Suo, *Journal of Materials Research*, **25**, 1007 (2010).
7. X. Zhang, A. M. Sastry, and W. Shyy, *Journal of The Electrochemical Society*, **155**, A542 (2008).
8. J. Christensen and J. Newman, *Journal of The Electrochemical Society*, **153**, A1019 (2006).
9. J. Park, W. Lu, and A. M. Sastry, *Journal of The Electrochemical Society*, **158**, A201 (2011).
10. A. Paolone, R. Cantelli, G. Rousse, and C. Masquelier, *Journal of Physics: Condensed Matter*, **15**, 457 (2003).
11. J. Sugiyamat, T. Tamura, and H. Yamauchi, *Journal of Physics: Condensed Matter*, **7**, 9755 (1995).
12. P. Piszora, *Zeitschrift für Kristallographie Supplements*, **2007**, 387 (2007).
13. Y. Lin, Y. Yang, H. Ma, Y. Cui, and W. L. Mao, *The Journal of Physical Chemistry C*, **115**, 9844 (2011).
14. G. E. Grechnev, R. Ahuja, B. Johansson, and O. Eriksson, *Physical Review B*, **65**, 174408 (2002).
15. T. Maxisch and G. Ceder, *Physical Review B*, **73**, 174112 (2006).
16. Y. Qi, H. Guo, L. G. Hector, and A. Timmons, *Journal of The Electrochemical Society*, **157**, A558 (2010).
17. T. Ohzuku, M. Kitagawa, and T. Hirai, *Journal of The Electrochemical Society*, **137**, 769 (1990).
18. K. Kanamura, H. Naito, T. Yao, and Z.-i. Takehara, *Journal of Materials Chemistry*, **6**, 33 (1996).
19. Y. Xia and M. Yoshio, *Journal of The Electrochemical Society*, **143**, 825 (1996).
20. W. Liu, K. Kowal, and G. C. Farrington, *Journal of The Electrochemical Society*, **145**, 459 (1998).
21. I. Yoshiaki, *Physics of the Earth and Planetary Interiors*, **13**, 97 (1976).
22. K. Suzuki, Y. Oumi, S. Takami, M. Kubo, A. Miyamoto, M. Kikuchi, N. Yamazaki, and M. Mita, *Japanese Journal of Applied Physics*, **39**, 4318 (2000).
23. K. Tateishi, D. du Boulay, N. Ishizawa, and K. Kawamura, *Journal of Solid State Chemistry*, **174**, 175 (2003).
24. K. Tateishi, D. d. Boulay, and N. Ishizawa, *Applied Physics Letters*, **84**, 529 (2004).
25. P. Steve, *Journal of Computational Physics*, **117**, 1 (1995).
26. A. K. Subramaniyan and C. T. Sun, *International Journal of Solids and Structures*, **45**, 4340 (2008).
27. A. Adnan, C. T. Sun, and H. Mahfuz, *Composites Science and Technology*, **67**, 348 (2007).
28. D. Ravinder, *Journal of Applied Physics*, **75**, 6121 (1994).
29. Y. Shiraishi, I. Nakai, T. Tsubata, T. Himeda, and F. Nishikawa, *Journal of Solid State Chemistry*, **133**, 587 (1997).
30. M. B. Kruger, J. H. Nguyen, W. Caldwell, and R. Jeanloz, *Physical Review B*, **56**, 1 (1997).
31. S. Åsbrink, A. Waśkowska, J. S. Olsen, and L. Gerward, *Physical Review B*, **57**, 4972 (1998).
32. S. Åsbrink, A. Waśkowska, L. Gerward, J. Staun Olsen, and E. Talik, *Physical Review B*, **60**, 12651 (1999).
33. A. Waskowska, L. Gerward, J. S. Olsen, S. Steenstrup, and E. Talik, *Journal of Physics: Condensed Matter*, **13**, 2549 (2001).